Chapter 2
Photonic Plasma Instabilities and Soliton Turbulence in Spatially Incoherent Light

Dmitry V. Dylov and Jason W. Fleischer

Abstract We develop a plasma theory of nonlinear statistical optics. In this model, partially spatially incoherent light is treated as an ensemble of speckles which can interact through the nonlinearity. A photonic plasma frequency is defined, as is a photonic Debye length. This approach unifies previous observations using partially coherent light and predicts a new class of optical phenomena. Examples include the two-scale energy transfer common to modulation instability and the continuous excitation of modes from the gradient-driven bump-on-tail instability. The latter example, well-known from plasma physics, represents a new regime for optical experiments. We observe it here by considering the nonlinear coupling of two partially coherent beams in a self-focusing photorefractive crystal. For weak wave coupling, determined by small modal density within a Debye sphere, we observe momentum exchange with no variation in intensity. For strong wave coupling, modulations in intensity appear, as does evidence for wave (Langmuir) collapse at large scales.

To achieve a broader range of wave coupling, we consider a double bump-on-tail geometry. This system can be modeled as a pair of coupled single-hump instabilities whose interaction involves general issues of nonlinear competition, synchronization, etc. For the case of strong wave coupling, the multiple humps merge into a single-peaked profile with an algebraic k^{-2} inertial range. This self-similar spectrum, representing an ensemble of dynamically-interacting solitons atop a sea of radiation modes, is a definitive observation of soliton (Langmuir) turbulence.

Dmitry V. Dylov
Department of Electrical Engineering, Princeton University, Olden Street, Princeton, New Jersey 08544, USA, e-mail: dvd@princeton.edu

Jason W. Fleischer
Department of Electrical Engineering, Princeton University, Olden Street, Princeton, New Jersey 08544, USA, e-mail: jasonf@princeton.edu

O. Descalzi et al. (eds.), *Localized States in Physics: Solitons and Patterns*,
DOI 10.1007/978-3-642-16549-8_2,

2.1 Introduction

Dynamical instabilities occur in every nonlinear wave system. Perhaps the simplest is modulation instability (MI), in which perturbations grow at the expense of a uniform background. For example, a plane wave propagating in a self-focusing medium will break up into stripes, with a characteristic period determined by a balance between diffraction/dispersion and nonlinearity. If the background is statistical, *e.g.* thermal, then attempts at growth are de-phased by the background, and there is a nonlinear threshold for instability [1, 2, 3, 4]. Put another way, mode coupling must be sufficiently strong to generate enough correlation for unstable growth. Once instability begins, the evolution is again characterized by a direct transfer between the background and a preferred scale (this time determined by the correlation length). The resulting array of solitons is then free to interact over longer evolution times/propagation distances.

A contrasting process of energy transfer is one that occurs over a continuum of scales. This type of dynamics involves a local coupling between adjacent modes in wavenumber space, resulting in a self-similar cascade. This process gives an algebraic power spectrum and is typical of homogeneous turbulence, such as that described by Kolmogorov theory [5, 6]. It is simpler, in some senses, as dimensional analysis and scaling arguments can be used to characterize the dynamics.

The two methods of energy transfer represent complementary limits. Two-scale coupling can cascade, with higher-order effects appearing. This includes the generation of higher-order modes [7], condensation processes [8, 9, 10], and soliton clustering [11]. Likewise, local coupling can generate localized structures which can evolve dynamically [5, 12, 13]. This convergence of dynamics should not be surprising, as they are nothing but different pathways to the same asymptotic state.

Until recently [14, 15, 16, 7, 17, 18], only two-scale dynamics had been demonstrated experimentally in optics, *viz.* the snake instability in self-defocusing media [19] and modulation instability in self-focusing media [3, 4]. Here, we outline our work on instabilities which cascade modes over a range of scales. As optical turbulence is our ultimate goal, we use light that is partially spatially incoherent. Such beams can be treated as an ensemble of speckles which, in a nonlinear medium, can be considered as quasi-particles that interact through large-scale modulation waves [14]. This description gives rise to a photonic plasma interpretation. It unifies all previous observation in nonlinear statistical optics and predicts a wide range of new dynamics.

As a particular example, we consider an all-optical bump-on-tail instability. This instability, well-known in plasma physics [8, 9], is a *gradient-driven* effect which couples modes across a range of scales. We show that instability occurs whenever higher-momentum modes are more populated than lower ones, regardless of nonlinear coupling strength, and derive analytic dispersion relations for the growth rates. Experimentally, we observe the dynamics by considering the nonlinear coupling of two partially-coherent beams in a self-focusing photorefractive medium. For weak nonlinear interactions, the result is momentum (k) transfer without any observable

variation in intensity (x). For strong interactions, both x-space modulations and k-space dynamics appear.

As the dynamics evolve, the growing perturbations start to back-react on their underlying source distribution. The source intensity becomes depleted and its spectral profile is modified. For this stage, linear theory is no longer adequate. To address this, we develop a quasi-linear theory and apply it to the bump-on-tail example, showing explicitly how modes grow until there is no more driving gradient. For even stronger wave growth, wave-wave interactions become dominant. That is, the perturbed modes interact with each other, independent of the background distribution. This is a highly nonlinear state, and it is difficult to achieve experimentally with limited nonlinearity and propagation distance. To facilitate the process, we consider a double bump-on-tail geometry, so that a broader range of unstable wavenumbers can grow and interact. We show that the dynamics can be treated as a coupled pair of individual bump-on-tail instabilities. It is thus a model system which can address a variety of general issues in nonlinear dynamics, including synchronization, competition, parametric pumping, and cascades of energy and momentum transfer [20]. In our case, we show analytically and experimentally that the momentum cascade leads to an algebraic k^{-2} power spectrum. The results highlight the difficulty of synchronized wave mixing inherent in noisy nonlinear systems and demonstrate a pathway towards all-optical studies of turbulence.

2.2 Basic Theory and Formalism

Our starting equation is the nonlinear Shrödinger equation (NLS) for the slowly varying, partially coherent field packet $\psi(\boldsymbol{r},z)$, which reads

$$i\frac{\partial\psi}{\partial z}+\frac{\beta}{2}\nabla_{\boldsymbol{r}}^2\psi+\kappa G(\langle\psi^*\psi\rangle)\psi=0. \tag{2.1}$$

Here, $\boldsymbol{r}$ is a diffraction\dispersion variable, the propagation is along z and coefficient $\beta=\lambda/2\pi n_0$ is the diffraction (or second-order dispersion) coefficient for light of wavelength λ in a medium with base index of refraction n_0, κ is the nonlinear coefficient, and $G(\langle\psi^*\psi\rangle)$ is the nonlinear response function of the medium. The bracket $\langle...\rangle$ denotes statistical ensemble average; it is valid when the medium's response time is much longer than the characteristic time of the intensity fluctuations of the statistical wave packet.

2.2.1 Wigner Formalism

There are many equivalent ways to treat such partially coherent light [21]; here, we use a full wave-kinetic approach via the Wigner formalism [22, 23]. In this

method Eq. (2.1) is transformed by the Wigner function (including the Klimontovich statistical average), defined as

$$f(\boldsymbol{r},\boldsymbol{k},z) = (2\pi)^{-3}\int_{-\infty}^{+\infty} d^3\boldsymbol{\xi}\cdot e^{i\boldsymbol{k}\cdot\boldsymbol{\xi}}\left\langle \psi^*\left(\boldsymbol{r}+\frac{\boldsymbol{\xi}}{2}\right)\psi\left(\boldsymbol{r}-\frac{\boldsymbol{\xi}}{2}\right)\right\rangle. \tag{2.2}$$

Equation (2.2) satisfies the intensity relation $\langle\psi^*(\boldsymbol{r},z)\psi(\boldsymbol{r},z)\rangle = \int_{-\infty}^{+\infty} d^3\boldsymbol{k} f(\boldsymbol{r},\boldsymbol{k},z)$. Eq. (2.1) transformed by (2.2) takes the following form [22, 23, 24, 25, 14]

$$\frac{\partial f}{\partial z} + \beta\boldsymbol{k}\cdot\nabla_{\boldsymbol{r}} f + 2\kappa G\left(\langle\mid\psi\mid^2\rangle\right)\left[\sin\left(\frac{1}{2}\frac{\overleftarrow{\partial}}{\partial\boldsymbol{r}}\cdot\frac{\overrightarrow{\partial}}{\partial\boldsymbol{k}}\right)\right] f = 0, \tag{2.3}$$

where the arrows in the sine operator indicate that the spatial derivative acts on the function G (to the left) and the momentum derivative acts on the distribution f (to the right) [24, 25].

In the geometrical optics approximation (the long-wavelength limit): $\Delta\boldsymbol{k}\cdot\Delta\boldsymbol{r} \gg 2\pi$), so that Eq. (2.3) reduces to

$$\frac{\partial f}{\partial z} + \beta\boldsymbol{k}\cdot\nabla_{\boldsymbol{r}} f - \kappa\mathscr{E}(\boldsymbol{r},z)\cdot\nabla_{\boldsymbol{k}} f = 0, \tag{2.4}$$

where the self-consistent driving field $\mathscr{E}(\boldsymbol{r},z)$ is introduced as

$$\mathscr{E}(\boldsymbol{r},z) = -\nabla_{\boldsymbol{r}} G\left(\langle\mid\psi\mid^2\rangle\right). \tag{2.5}$$

Equation (2.3) is known as a Wigner-Moyal equation for the evolution of the Wigner distribution function $f(\boldsymbol{r},\boldsymbol{k},z)$. Its simplification (2.4) has a form of the Vlasov transfer equation [8, 24] or, essentially, a radiation transfer equation [26, 27, 21]. It is valid for slow (long-wavelength) variations in the refractive index when the average speckle size (correlation length l_c) of the light is smaller than the beam envelope. Note that the usual form of this short-wave–long-wave dynamics is coupled but has been reduced to a single equation by implicitly absorbing intensity fluctuations in $G\left(\langle\mid\psi\mid^2\rangle\right)$. Equation (2.4) implies the conservation of the number of optical quasi-particles in $\{\boldsymbol{r},\boldsymbol{k}\}$-space. In this chapter we will treat these quasi-particles collectively and borrow language from plasma physics. Eqs. (2.4), (2.5) then become a starting point to account for spectral dynamics of localization, oscillations and instabilities in statistical, nonlinear optics.

In plasma physics the self-consistent driving field defined in (2.5) is responsible for ponderomotive self-focusing, corresponding to the drift of electrons down a gradient in the plasma density [8, 6, 28, 29]. The corresponding nonlinear index change can be viewed as a divergence (variation) of $\mathscr{E}(\boldsymbol{r},z)$ resulting from the local intensity inhomogeneity. Mathematically we can express it in terms of the generic condition for $G(\langle\psi^*\psi\rangle)$:

$$\nabla_{\boldsymbol{r}}\cdot\mathscr{E}(\boldsymbol{r},z) = \kappa\left(\langle I_0\rangle - \int_{-\infty}^{+\infty} d^3\boldsymbol{k} f(\boldsymbol{r},\boldsymbol{k},z)\right), \tag{2.6}$$

where $\langle I_0 \rangle$ is a uniform background intensity without any variations. Equation (2.6) is a Poisson equation [8] that implies that nonlinearity acts as a uniformly distributed volumetric "charge". It is valid if the following physically sensible conditions are met: the right-hand side has to be finite, the functions G and $\mathscr{E}$ have to be spatially continuous, and the medium has to have only smooth optical inhomogeneities (if any).

2.2.2 Initial Stages of Instability. Linear Perturbation Theory

Initial stages of instabilities in nonlinear media can be studied by standard perturbation analysis. To illustrate the main points, we consider perturbations around a spatially uniform distribution $f_0(\boldsymbol{k})$:

$$f(\boldsymbol{r},\boldsymbol{k},z) = f_0(\boldsymbol{k}) + \sum_{\boldsymbol{\alpha}} \rho_{\boldsymbol{\alpha}}(\boldsymbol{k},z) e^{i\boldsymbol{\alpha}\cdot\boldsymbol{r}}, \tag{2.7}$$

with $|\,\rho_{\boldsymbol{\alpha}}\,| \ll |\,f_0\,|$ for all wavenumbers $\boldsymbol{\alpha} \neq 0$. In the unperturbed state, the nonlinear driving field (2.5) is assumed to be zero, so that $\mathscr{E}(\boldsymbol{r},z)$ can be regarded as a small quantity (weak nonlinearity). In terms of the Fourier modes,

$$\mathscr{E}(\boldsymbol{r},z) = \sum_{\boldsymbol{\alpha}} \mathscr{E}_{\boldsymbol{\alpha}}(z) e^{i\boldsymbol{\alpha}\cdot\boldsymbol{r}}. \tag{2.8}$$

Substituting (10.1) and (2.8) in Eqs. (2.4) and (2.6), noting that $\int_{-\infty}^{+\infty} d^3\boldsymbol{k} f_0(\boldsymbol{k}) = \langle I_0 \rangle$, and linearizing in the perturbations yields

$$\frac{\partial \rho_{\boldsymbol{\alpha}}}{\partial z} + i\beta\,\boldsymbol{\alpha}\cdot\boldsymbol{k}\,\rho_{\boldsymbol{\alpha}} - \kappa \mathscr{E}_{\boldsymbol{\alpha}} \cdot \nabla_{\boldsymbol{k}} f_0 = 0, \tag{2.9}$$

$$\mathscr{E}_{\boldsymbol{\alpha}} = \frac{\kappa}{\alpha^2} i\boldsymbol{\alpha} \int_{-\infty}^{+\infty} d^3\boldsymbol{k}\,\rho_{\boldsymbol{\alpha}}. \tag{2.10}$$

One can solve these equations using the Laplace transformation along the propagation coordinate ($\sim e^{gz}$). The resulting dispersion function is

$$D_{\boldsymbol{\alpha}}(g) = 1 + \frac{\kappa^2}{\alpha^2\beta} \int_{-\infty}^{+\infty} d^3\boldsymbol{k} \frac{\boldsymbol{\alpha}\cdot\nabla_{\boldsymbol{k}} f_0}{ig - \boldsymbol{\alpha}\cdot\boldsymbol{k}}. \tag{2.11}$$

The stability of the partially coherent beam in a nonlinear medium is then determined by the zeros in g of the dispersion function (2.11).

2.2.3 Growth Rate and Conditions for Weak/Strong Turbulence

For simplicity, we reduce the problem to one transverse dimension. The dispersion relation (2.11) becomes [3, 24, 30, 25, 14]

$$D_\alpha(g) = 1 + \frac{\kappa^2}{\alpha\beta}\int_{-\infty}^{+\infty} dk \frac{\partial f_0/\partial k}{ig - \alpha k}. \tag{2.12}$$

Initially, the function $D_\alpha(g)$ is defined for Re $g > 0$ and then is analytically continued into the rest of the plane. If there is a complex root $g(\alpha) = g_R(\alpha) - ig_I(\alpha)$ of $D_\alpha(g) = 0$, and $g_R(\alpha) > 0$, then any intensity perturbation will grow exponentially (instability).

A Lorentzian distribution $f_0(k) = (I_0 \Delta k/\pi)/\left(k^2 + \Delta k^2\right)$ plugged into Eq. (2.12) allows an exact solution to the growth rate:

$$\frac{g}{\beta\alpha^2} = -\Delta k + \frac{\alpha}{2}\sqrt{\frac{4\kappa I_0}{\beta\alpha^2} - 1}, \tag{2.13}$$

where $\Delta k = 2\pi/l_c$ represents the spectral spread for a beam with correlation length l_c. This gain coefficient, similar to that originally derived in Ref. [3], separates the effects of nonlinearity and statistics and shows a clear threshold value for the development of perturbations. As in plasma physics [1, 2], modulations will not appear unless the nonlinearity Δn is greater than the angular spread (effective temperature) $(\Delta k/k_0)^2$. Below threshold, modulations are suppressed, a de-phasing which Fedele and Anderson *et al.* interpreted as a type of Landau damping due to the monotonically-decreasing distribution f_0 [30, 24, 25]. However, they did not identify plasma-like parameters or consider the potential for inverse Landau damping (wave growth) when the distribution is non-monotonic.

To treat the gradient-driven dynamics at initial stages of instability, we consider first weak growth ($|g_R| \ll |g_I|$) in the long-wavelength limit ($|ig| \gg \alpha k$). Expanding the denominator in Eq. (2.12) then gives

$$\frac{g^2}{\beta\alpha^2} \approx \kappa \int_{-\infty}^{+\infty} dk\, f_0(k) \left[1 + 3\left(\frac{\alpha\beta}{g}\right)^2 k^2\right]. \tag{2.14}$$

To be consistent with the quasi-thermal light used in the experiment [31], we consider a Gaussian beam profile (the detailed difference between this distribution and a Lorentzian will be addressed in Section 2.4 below):

$$f_0(k) = \frac{I_0}{\sqrt{2\pi}\,\Delta k}\exp\left(-\frac{k^2}{2\Delta k^2}\right). \tag{2.15}$$

Note that a Lorentzian distribution will give the same results below, though more care is needed to handle the divergence of $\langle k^2\rangle$ in Eq. (2.14). The form (2.15) of the intensity is more true to the plasma mapping [18], in which the underlying

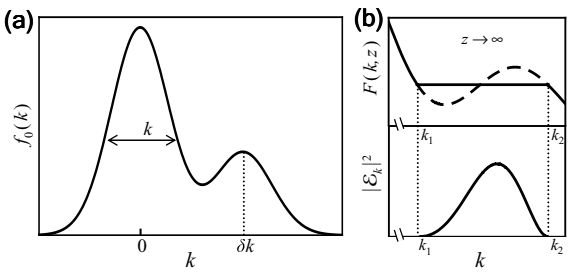

Fig. 2.1 Quasi-thermal unstable light. (a) Typical double-hump distribution in k-space for BOT instability. (b) Asymptotic quasi-linear plateau and corresponding spectral energy density in the unstable region $k_1 \le k \le k_2$.

distribution is Maxwell-Boltzmann. We note, however, that there is no true equilibrium distribution in the optical system, as there are no collisions available for relaxation [32]. Put another way, the dynamical system (2.4) conserves entropy, so that there are many possible steady-state profiles with which to start.

Explicitly accounting for the principal value and pole in Eq. (2.14) gives

$$g(\alpha) = ig_p\left(1+\frac{3}{2}\alpha^2\lambda_D^2\right) + \frac{\pi}{2}\kappa\alpha\sqrt{\frac{\kappa I_0}{\beta}}\left(\frac{\partial f_0}{\partial k}\right)\Big|_{k=g_p/\alpha\beta}, \tag{2.16}$$

where g_p is an effective plasma frequency and λ_D is an effective Debye length, with $\alpha\lambda_D \ll 1$. These parameters are

$$g_p = \sqrt{\frac{\kappa I_0}{\beta}}\,, \qquad \lambda_D = \frac{\beta\Delta k}{g_p}\,. \tag{2.17}$$

The first term in Eq. (2.17) is a Bohm-Gross dispersion relation [8] for nonlinear statistical light, showing that optical speckles can interact via Langmuir-type waves [14, 18]. Growth or damping of these waves is a resonant process that depends on the relative (spatial) phase velocity of the underlying quasi-particles (speckles). From the second term in Eq. (2.16), it is clear that there are no growing modes if $\partial f_0/\partial k < 0$, *e.g.*, for a quasi-thermal Gaussian distribution, since on average more quasi-particles travel slower than the interaction wave than faster. However, the weak limit used to derive (2.16) breaks down when $\alpha\lambda_D \approx 1$, or $\kappa I_0 \approx \beta\langle\Delta k^2\rangle$; in this case case, the growth rate exceeds the rate of statistical dephasing (spectral bandwidth) of the background, causing intensity modulations to appear [1, 9]. Interestingly, this strong-coupling condition becomes the instability threshold reported earlier in [3].

Not considered before, however, was the possibility for optical instability by inverse Landau damping when $\partial f_0/\partial k > 0$ (see Fig. 2.1(a) for a typical distribution). A prime example is the "bump-on-tail" (BOT) instability, well-known from plasma physics [8], in which a non-equilibrium hump is added to one side of an equilibrium distribution. To our knowledge, the BOT instability has never before been demonstrated outside of a plasma context. However, it should be clear from the above

derivation that BOT dynamics should occur in any wave-kinetic system, including hydrodynamics [33], optics, and (potentially) Bose-Einstein condensates.

The dynamics within this photonic plasma depend on the spectral density of perturbation modes within a Debye sphere. For the weak-coupling regime considered above, defined by $\alpha\lambda_D \ll 1$ [1, 9, 3], the BOT instability is mostly a momentum-space effect [14]. Above this threshold, intensity modulations appear [1, 34, 3, 4], wave-wave coupling (*vs.* wave-speckle coupling) becomes dominant [14, 10, 9], and the perturbation method ceases to apply. Adopting plasma language, we define these two limits as regimes of *weak* and *strong* optical Langmuir turbulence [15].

2.2.4 Debye Scaling

In all previous work, the statistics of the input beam and the nonlinearity of the medium have been considered separate parameters, as they are controlled separately in the experiments. However, Eq. (2.16) shows that they are joined in the composite parameter of the photonic Debye length λ_D. As in material plasma, λ_D signifies the amount of interaction wave inhibition (screening) due to the random de-phasing of waves [14].

The photonic Debye length provides a natural length scale for highly incoherent beams, *i.e.* beam for which the correlation length is significantly less than the beam width ($l_c \ll w_0$). For example, narrow (Gaussian) beams that linearly expand as $(w(z)/w_0)^2 = 1+\bar{z}^2$, where $\bar{z} = z/L_D$ is the propagation distance measured in terms of the linear diffraction length L_D, evolve nonlinearly as

$$\left(\frac{w(z)}{w_0}\right)^2 = 1+\bar{z}^2\left(1-\bar{\lambda}_D^2\right), \tag{2.18}$$

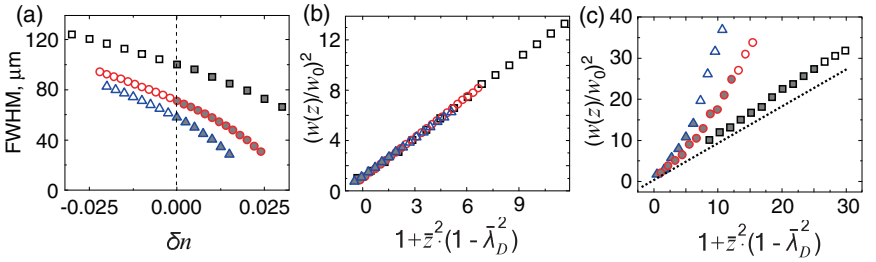

Fig. 2.2 Numerical and eperimental results for the nonlinear diffraction of a spatially incoherent beam. (a) Plot of full-width half-maximum versus δn at a fixed propagation distance $z = 1cm$. (b) Plot of simulation results in (a) using scaling from Eq. (2.18); (c) Experimental results measured after propagation in a photorefractive crystal. The dashed line represents the highly-incoherent limit of Eq. (2.18).

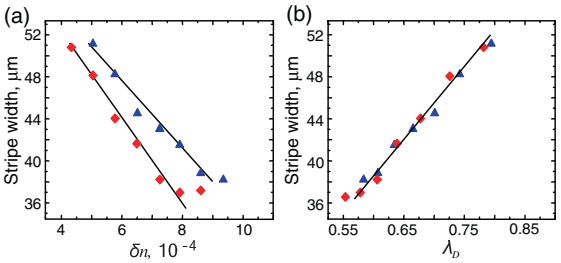

Fig. 2.3 Period of MI pattern ("stripe width") as a function of (a) nonlinearity and (b) Debye length. Data for two correlation lengths of $80\mu m$ (triangles) and $92\mu m$ (rhombus) are shown. Notice the collapse of data after Debye scaling.

where $\overline{\lambda}_D$ is the Debye length normalized to the nonlinear length that characterizes a coherent soliton [35]. Numerical and experimental verification of this formula, for nonlinearities below the soliton limit, are shown in Fig. 2.2.

Technically, the plasma formula (2.16) is only valid for weak perturbations, for which $|g_R| \ll |g_I|$. On the other hand, it is reasonable to use the Langmuir modes from this theory as a basis for further interactions when the nonlinearity is increased [12, 13]. This suggests that the Debye length remains a valid scaling parameter. As shown in Fig. 2.3 for the case of incoherent modulation instability, this is indeed the case.

Finally, these results can be generalized to more complex cases. For example, multiple-stream geometries in k-space can be represented in terms of Gaussian multi-hump distribution, with the "humps" positioned at different spatial frequencies (angular separations) δk_{01}, δk_{12}, δk_{23},...,$\delta k_{M-1\,M}$:

$$f_0(k) = \frac{1}{\sqrt{2\pi}\,\Delta k}\left[I_0 e^{-\frac{k^2}{2\Delta k^2}} + \sum_{j=1}^{M} I_j \mathrm{e}^{-\frac{(k-\delta k_{j-1\,j})^2}{2\Delta k^2}}\right], \tag{2.19}$$

then the system's dynamics would still be described simply by Eq. (2.16), but with the Debye length scaled as [15]

$$\tilde{\lambda}_D = \sqrt{\frac{\beta^3}{\kappa}\left(\frac{\Delta k^2}{I_{tot}} + \sum_{j=1}^{M}\frac{\delta k_{j-1\,j}^2}{I_j}\right)}. \tag{2.20}$$

Note that due to the redistribution and reshaping of the total intensity $I_{tot} = \sum_j I_j$, the threshold for the appearance of intensity modulations will shift as well.

2.3 Quasi-Linear Approximation

It was mentioned in the Section 2.2.4 that after the initial steps of instability, linear perturbation theory ceases to be valid [14, 36, 37]. The reason is that the shape of distribution function changes with time, due to energy depletion and back-reaction by the perturbations. In this section we will treat such dynamics as time-dependent

(or, more rigorously, z-dependent), which means that it is necessary to consider evolution of perturbations as well.

2.3.1 General Derivation

We proceed by returning to the one-dimensional case of Eq. (2.4). Using the Fourier decompositions (10.1) and (2.8), we rewrite (2.10) as

$$\frac{\partial \rho_\alpha(k,z)}{\partial z} + i\beta\alpha k\rho_\alpha(k,z) - \kappa\mathscr{E}_\alpha(z)\frac{\partial(f_0(k)+\rho_0(k,z))}{\partial k} = 0, \tag{2.21}$$

where we neglected the wave-wave interaction term $\sum_{\alpha'\neq 0}\mathscr{E}_{\alpha-\alpha'}\partial_k\rho_{\alpha'}$ and took only first term ρ_0 to account for z-dependence of Wigner distribution function. We assume that ρ_0 is a slowly varying function of z, while f_0 is a distribution giving rise to a weak instability (like in the double-hump case of Fig. 2.1(a)). The rate of change of ρ_0 is given by

$$\frac{\partial \rho_0}{\partial z} = \sum_\alpha \mathscr{E}_{-\alpha}\frac{\partial \rho_\alpha}{\partial k}. \tag{2.22}$$

Now assume that ρ_α and $\mathscr{E}_\alpha$ have the following form:

$$\begin{aligned}\rho_\alpha(k,z) &= \hat{\rho}_\alpha(k)\exp\left(\int^z d\zeta[g_R(\zeta)-ig_I(\zeta)]\right),\\ \mathscr{E}_\alpha(z) &= \hat{\mathscr{E}}_\alpha\exp\left(\int^z d\zeta[g_R(\zeta)-ig_I(\zeta)]\right).\end{aligned} \tag{2.23}$$

The solution to (2.21) is then

$$\rho_\alpha = \frac{i\kappa}{\beta}\mathscr{E}_\alpha\frac{\partial/\partial k(f_0+\rho_0)}{ig_R+g_I-\alpha k}, \tag{2.24}$$

This result can be plugged into Poisson's equation, and analogous calculations of the dispersion relation and growth rate yield:

$$D_\alpha(g) = 1+\frac{\kappa^2}{\alpha\beta}\int_{-\infty}^{+\infty}dk\frac{\partial/\partial k(f_0+\rho_0)}{ig_R+g_I-\alpha k}, \tag{2.25}$$

$$g_R = \frac{\pi}{2}\kappa\alpha\sqrt{\frac{\kappa I_0}{\beta}}\left(\frac{\partial\,(f_0+\rho_0)}{\partial k}\right)\Bigg|_{k=g_p/\alpha\beta}. \tag{2.26}$$

Notice that g_R became a slowly varying function of z through ρ_0. The long-term processes can be studied now by examining the long-term behavior of ρ_0. For this we substitute Eq. (2.24) into Eq. (2.22), which gives

$$\frac{\partial \rho_0}{\partial z} = \frac{\kappa^2}{\beta^2} \sum_\alpha |\mathscr{E}_\alpha|^2 \frac{\partial}{\partial k} \left[\frac{g_R}{(g_I - \alpha k)^2 + g_R^2} \frac{\partial F}{\partial k} \right], \tag{2.27}$$

where we used $\mathscr{E}_\alpha = \mathscr{E}_{-\alpha}$, and $F(k,z) \equiv f_0(k) + \rho_0(k,z)$. Note that Eq. (2.27) has the form of a diffusion equation. Turning from sums to continuous integrals and using (2.23) we get

$$\frac{\partial F}{\partial z} = \frac{\partial}{\partial k} \left(D_k \frac{\partial F}{\partial k} \right), \tag{2.28}$$

$$\frac{\partial |\mathscr{E}_\alpha|^2}{\partial z} = 2 g_R |\mathscr{E}_\alpha|^2, \tag{2.29}$$

where the k-space diffusion function is defined as

$$D_k = \frac{\kappa^2}{\beta^2} \int_{-\infty}^{+\infty} d\alpha |\mathscr{E}_\alpha|^2 \frac{g_R}{(g_I - \alpha k)^2 + g_R^2}. \tag{2.30}$$

Eqs. (2.28) and (2.29) are the basic equations of quasi-linear theory for statistical light. They govern the rate of change of the distribution F and spectral energy density $|\mathscr{E}_\alpha|^2$ as the light propagates in a moderately nonlinear medium.

2.3.2 Bump-on-Tail Dynamics

We now apply the quasi-linear formalism to the bump-on-tail instability shown in Fig. 2.1. Previously thought to exist only in plasma, the bump-on-tail (BOT) instability is a gradient-driven effect in which a non-equilibrium bump on the tail of a thermal distribution acts as a source of free energy [8]. As such, it requires an inverted population of statistical modes and is often considered a type of classical lasing [38]. In plasma, the effect occurs when a gas of charged particles interact through electrostatic, or Langmuir, waves. Recently, we showed that the same phenomenon could occur in the nonlinear propagation of statistical light, in which an ensemble of speckles interact through large-scale modulation waves [14].

The initial distribution may be written as

$$f_0(k) = \frac{I_0}{\sqrt{2\pi}\,\Delta k} \exp\left(-\frac{k^2}{2\Delta k^2} \right) + \frac{I_1}{\sqrt{2\pi}\,\Delta k} \exp\left(-\frac{(k-\delta k)^2}{2\Delta k^2} \right), \tag{2.31}$$

with $I_1 < I_0$ and $\delta k \geq \Delta k$. Theoretically, initial stages of BOT instability can be fully described by (2.16), with

$$g_p = \sqrt{\frac{\kappa(I_0 + I_1)}{\beta}}\ ,\ \lambda_D = \sqrt{\frac{\beta^3}{\kappa} \left(\frac{\Delta k^2}{I_0 + I_1} + \frac{\delta k^2}{I_1} \right)}\ . \tag{2.32}$$

This linearized theory, however, says nothing about the progression of the distribution after some distance of propagation, such as saturation (stabilization) of continued instability; it merely provides wavenumbers of unstable modes between the beams. The deficiency of standard linearized theory is that it considers $f_0(k)$ z-independent, which is no longer valid as the dynamics evolve.

Recalling that $|g_R| \ll |g_I|$, the fraction in the diffusion function (2.30) can be approximated as $\sim \pi\delta(g_I - \alpha k)$, yielding

$$\frac{\partial F}{\partial z} = \frac{\kappa^2}{\beta^2}\frac{\partial}{\partial k}\left[\frac{1}{|k|}|\mathscr{E}_k|^2\frac{\partial F}{\partial k}\right]. \tag{2.33}$$

The asymptotic state of the instability can be found by considering the change of the corresponding power spectrum $W(z) = 1/2\int dkF^2(k,z)$. Using (2.33), we have

$$\frac{\partial W}{\partial z} = \int_{-\infty}^{+\infty} dkF\frac{\partial F}{\partial z} = -\frac{\kappa^2}{\beta^2}\int_{-\infty}^{+\infty} dk\frac{1}{|k|}|\mathscr{E}_k|^2\left(\frac{\partial F}{\partial k}\right)^2. \tag{2.34}$$

Each term in the last integrand is positive, which means that W will decrease until either $|\mathscr{E}_k|^2 = 0$, or $\partial F/\partial k = 0$ for each value of k. The initial growth of modes is described by (2.16) and (2.32), and since $|\mathscr{E}_k|^2$ grows in the region between the two beams, the distribution function should flatten out so that there is no driving gradient $\partial F/\partial k$ (Fig. 2.1(b)). This "quasi-linear plateau" has been observed in recent experiments [14, 15] (to be discussed in Section 2.5).

Lastly, using (2.16), (2.32), and (2.33) and neglecting $\partial|\mathscr{E}_k|^2/\partial k$ at $z = 0$, we can calculate the asymptotic values of $|\mathscr{E}_k|^2$ and F as

$$|\mathscr{E}_k|^2\Big|_{z=\infty} = \frac{\pi\beta}{g_p}k^3\int_{k_1}^{k} dk[F(k,\infty) - f_0(k)], \tag{2.35}$$

$$F(k,\infty) = \frac{1}{k_2 - k_1}\int_{k_1}^{k_2} dkf_0(k), \tag{2.36}$$

where k_1 and k_2 are the k-vectors of the unstable region, $k_1 \le k \le k_2$, in which the plateau is established (see Fig. 2.1(b)). Expressions (2.35) and (2.36) provide the the effective overall gain of the flattening and the hight of the resulting plateau.

2.4 Numerical Analysis

2.4.1 Numerical Results for BOT Instability

To check the validity of the Quasi-Linear Approximation and Eqs. (2.35), (2.36), we have carried out numerical simulations of Eq. (2.4) and (2.5) for the case of a Kerr medium (Fig. 2.4). The bump-on-tail configuration was created by launching two partially incoherent beams of fixed spectral width $\Delta k/k_0 = 1.7\times10^{-3}$ at a

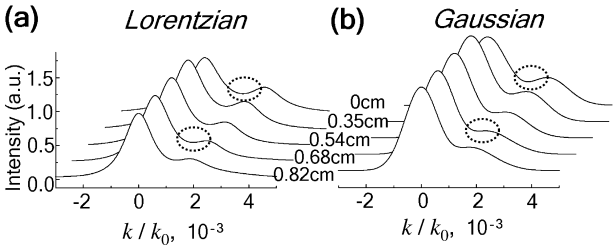

Fig. 2.4 Simulation of bump-on-tail propagation in a nonlinear Kerr-like medium. Shown are double-hump spectra for (a) Lorentzian and (b) Gaussian distributions. The total intensity and nonlinearity are kept constant ($\Delta n/n_0 = 1.74 \times 10^{-4}$) and only the shape of the statistics differs. Dashed circles highlight the initial driving gradient and formation of the quasilinear plateau, which occurs quicker in the Gaussian case.

relative angles $\delta k/k_0 = 2.0 \times 10^{-3}$. Comparisons between Lorentzian and Gaussian profiles for the distribution $f_0(k)$, at fixed total intensity $\langle I_0 \rangle$, show that the Gaussian distribution triggers the unstable dynamics faster. More details of this momentum transfer will be discussed in Section 2.5.

2.4.2 Numerical Results for Multiple BOT Instability

Figure 2.5 shows numerical simulation of the dynamics and the corresponding gain curves calculated from Eqs. (2.16) and (2.20) when three beams are launched into the medium (multiple bump-on-tail instability). As expected, modes grow in the regions of positive spectral slope until there is no more driving gradient. We find that the system is described effectively as a pair of coupled BOT instabilities: one

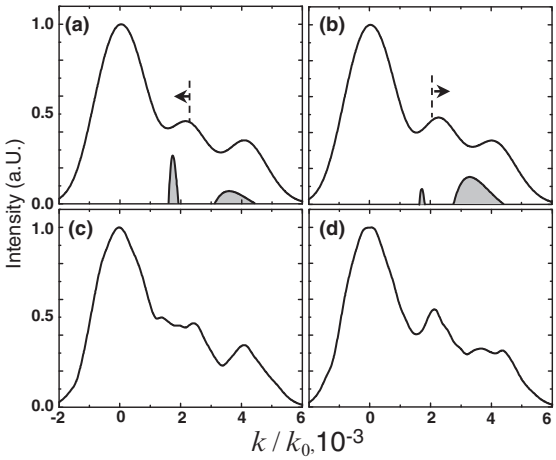

Fig. 2.5 Numerical simulation of multiple bump-on-tail instability. (a,b) Input profiles, with corresponding gain curves (shaded graphs at baseline), with the middle hump shifted (a) to the left of the equal gain value and (b) to the right. (c,d) Output pictures after $1cm$ of propagation ($\Delta n/n_0 = 1.74 \times 10^{-4}$).

on the left and one on the right, with negligible coupling between the leftmost and rightmost Gaussians due to their separation distance [15]. In this case, competition between the gain curves implies that plateau formation happens sequentially, even though the initial slopes and nonlinearity in the two regions are identical. If the middle hump is closer to the left (main) distribution, then the left region goes unstable first, and vice versa with a right bias (Figs. 2.5(c,d)). The balanced situation, with the central hump equidistant from either side, has gain curves of the same peak value and is unstable. In simulations, this initial condition always degenerated into one of the two asymmetric scenarios, a result supported by analytic perturbations of δk_{01} in Eq. (2.16).

2.5 Experimental Observation

2.5.1 Experimental Setup

Experimentally, we explore the bump-on-tail dynamics by considering the nonlinear interaction of two partially-coherent spatial beams. The setup is shown in Fig. 2.6. A statistical light input is created by focusing light from a 532*nm* CW laser onto a ground-glass diffuser and then imaging into a photorefractive SBN:60 ($Sr_{0.6}Ba_{0.4}Nb_2O_6$) crystal [31]. The correlation length, and correspondingly the spectral bandwidth, can be changed by varying the magnification properties of the imaging lens. To create a bump-on-tail or a double bump-on-tail distribution (Fig. 2.6, inset), the spatially-incoherent beam is split (one or more times) using a Mach-Zehnder interferometer, attenuated in the bump arm(s), and then recombined on the input face of the crystal.

For SBN, the nonlinear index change $\Delta n = \gamma E_{app}\langle I\rangle/(1+\langle I\rangle)$, where E_{app} is an electric field applied across the crystalline c-axis and $\gamma = n_0 r_{33}(1+\langle I_0\rangle)$ is a constant depending on the base index of refraction n_0, the electro-optic coefficient r_{33},

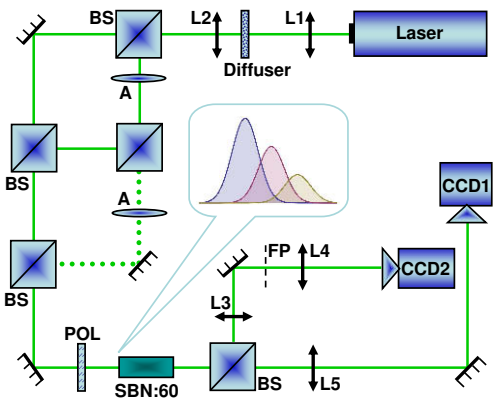

Fig. 2.6 Experimental Setup. 532*nm* laser light is made partially spatially incoherent by a ground-glass diffuser and separated into a superposition of two or three beams (for three, a dot-lined interferometer arm is added). A, attenuator; M, mirror; L, lens; BS, beam-splitter; POL, linear polarizer; SBN:60, nonlinear photorefractive crystal; FP, focal Fourier plane of the lens L3; CCD, digital detector.

and the spatially-homogeneous incident light intensity $\langle I_0 \rangle$ [27]. In the experiments, the beams have a relative angle of 0.3° (between any adjacent two beams), the intensity ratio is fixed at 3:2, and the strength of the nonlinearity (wave coupling) is controlled by varying the applied voltage (similar results occur at other angles and intensities). To observe the interaction, light exiting the crystal is directly imaged in both position (x) space and momentum (k) space, the latter by performing an optical Fourier transform.

For comparison and calibration, we performed a single-beam MI experiment with the main $\langle k \rangle = 0$ hump (not shown). In this case, the background distribution is Gaussian with a correlation length $l_c = 176\mu m$, and no intensity modulations appeared until the voltage reached $0.9kV$. Using $n_0 = 2.3$ and $r_{33} = 255pm/V$, this corresponds to a nonlinear index change of $\Delta n = 8 \times 10^{-4}$. Above this threshold, two symmetric momentum peaks appear at $k/k_0 = \pm 5.6 \times 10^{-3}$. This is the same behavior as in [4] but quantitatively calibrated to our initial input conditions and particular crystal.

2.5.2 Single Bump-on-Tail Instability

All-optical examples of a wave-kinetic bump-on-tail instability are shown in Figs. 2.7, 2.8 and 2.9. Figs. 2.7(a-f) show the behavior for weak interaction. In this case, the photorefractive nonlinearity is turned on by applying a $0.7kV$ voltage bias across the crystal, below the $0.9kV$ bias necessary to trigger single-beam MI. As shown in Figs. 2.7(c,f), nonlinear modes are excited precisely in the expected region of positive slope, growing until there is no more driving gradient (a process known as quasilinear flattening, see Section 2.3). Remarkably, the momentum-space distribution is changed [Figs. 2.7(e,f)] while the position-space intensity shows no observable variations [Fig. 2.7(d)].

The nature of the instability depends on the spectral geometry of the system. For a single-humped distribution [3], or one with widely-separated peaks [39], strong nonlinearity is required to see any significant dynamics. Here, the spectral peaks overlap, giving an unstable condition with $|g_R| \ll |g_I|$. The resulting momentum exchange, along with the resonance from Eq. (2.11), suggests that there is an underlying phase matching among the modes. Indeed, recent work with incoherent light in a medium with instantaneous (vs. inertial) nonlinearity shows an analogous velocity locking [40]. This demonstration, combined with similar momentum exchange observed in collisions of coherent vector solitons [41, 42], implies that the BOT dynamics should occur for true Kerr media as well. In the incoherent case considered here, the dynamics depends on the statistics of the interacting beams (Fig. 2.8). Local correlation measurements can reveal details of the speckle-wave coupling, but a simpler measure can be obtained from the visibility

$$\nu = (f(k_1) - f(k_{01}))/(f(k_1) + f(k_{01}))$$

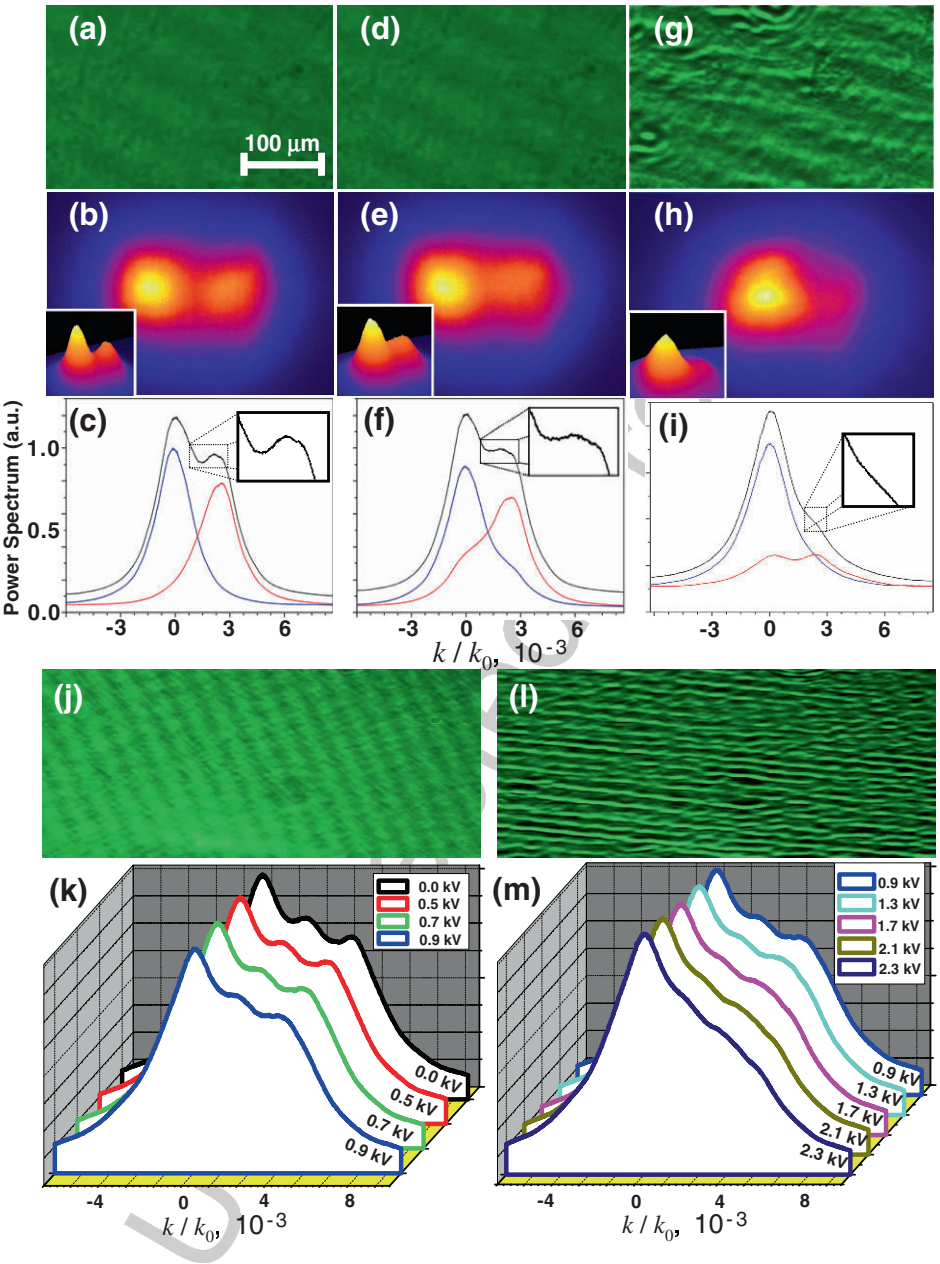

Fig. 2.7 Experimental output pictures of bump-on-tail and double bump-on-tail instability. (a,d,g,j,l) Intensity in position (x) space; (b,c,e,f,h,i,k,m) power spectrum in momentum (k) space. (a,b,c): crystals exit face after linear propagation of double-hump distribution (no applied voltage); (d,e,f): same, but nonlinear propagation (applied voltage of $0.7kV$, in the weak-coupling regime); (g,h,i) same, but in the strong-coupling regime ($1.6kV$). The blue and red curves in (c,f,i) show holographic readouts of single-beam propagation for the straight (blue) and angled (red) distributions, respectively. (j,k) Weak-coupling regime when the distribution is triple-humped. (l,m) Same, but in strong-coupling regime.

of the angled hump, as shown in Fig. 2.8(d). The efficiency of the flattening depends on the relative gain $|g_R|$ of the unstable modes. Using

$$\eta = (f_{NL}(k_{01}) - f_{Lin}(k_{01}))/(f_{NL}(k_0)) + f_{Lin}(k_0))$$

as a measure of efficiency, Fig. 2.8(e) shows interaction behavior that is relatively insensitive to nonlinear coupling strength but highly sensitive to beam statistics [14]. If the beam is too incoherent, then attempts at spectral energy transfer are de-phased. If the beam is too coherent, then the system loses its statistical nature (and thus its wave-kinetic properties). More rigorously, the first condition states that the angular separation between the beams must be greater than the spectral width of the distribution, while the second condition states that if the relative bandwidth is too small, then there are too few quasi-particles (speckles) in resonance with the growing waves [8, 9]. As a result, there is an optimal correlation length, for a given intensity ratio and angle given by $\partial g_R/\partial k = 0$, for efficient dynamical coupling.

For stronger nonlinearity, the system enters a regime of strong wave coupling, significantly distorting the original distribution in k-space and creating modulations in x-space (Figs. 2.7(g-i)). These modulations are different from those arising from MI, however, as the spectrum in Figs. 2.7(h,i) shows a range of modal excitation (between the original humps), rather than the symmetric high-k side lobes charac-

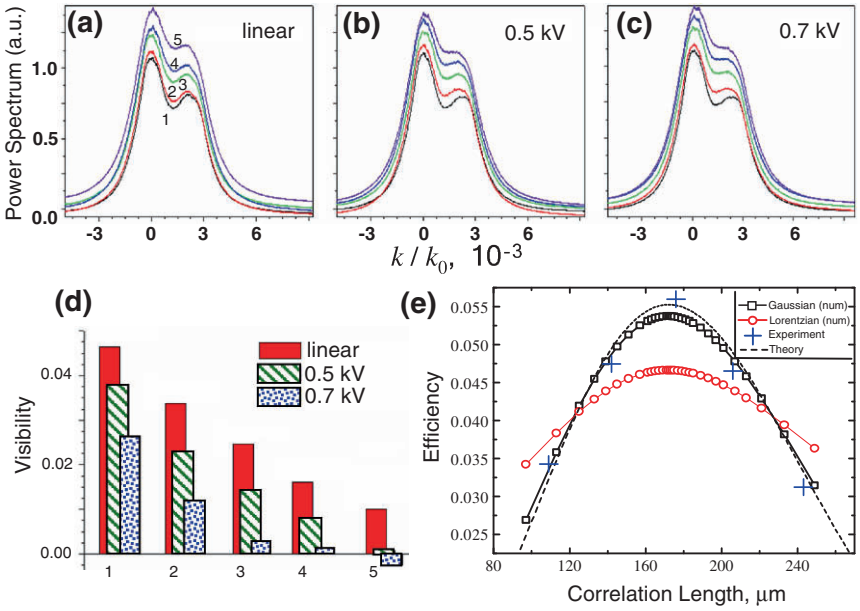

Fig. 2.8 Dynamical coupling as a function of correlation length and nonlinearity. (a-c) Power spectra at $0kV$ (linear), $0.5kV$ and $0.7kV$, respectively. (d) Visibility of the angled hump. (e) "Efficiency" of nonlinear flattening. Curves and bars in (a-d) are numbered for correlation lengths of $243\mu m$ (1), $206\mu m$ (2), $176\mu m$ (3), $142\mu m$ (4), and $109\mu m$ (5). Note the dependence of efficiency on the underlying distribution.

teristic of MI (*e.g.* [3, 43]). Using our reference correlation length $l_c = 176\mu m$, as in Fig. 2.7(a-f), we observe that the required nonlinearity for modulations is $1.1kV$, stronger than the one needed for single-beam MI. That is, the presence of a second statistical beam further suppresses the growth of modulations. Moreover, the appearance of modulations coincides with a breakdown of the quasilinear plateau and a resumption of wave growth in the unstable, non-equilibrium region [Fig. 2.7(i)].

The higher threshold can be understood by returning to the strong-coupling condition $\kappa I_0 \approx \beta\langle\Delta k^2\rangle$ obtained in Section 2.2. It is clear that for a given spectral width, additional intensity lowers the required value of κ for instability [3, 44]. However, the presence of a second beam increases the effective bandwidth due to cross-beam interaction, potentially requiring a higher value of κ. A simple estimate can be obtained by considering the variance of two Gaussian beams $\exp\left(-k^2/\Delta k^2\right) + A\exp\left(-(k-\delta k)^2/\Delta k^2\right)$, which is $\Delta k^2 + \delta k^2 A/(1+A)^2$. For $A = 2/3$ and $\delta k \sim \Delta k$, as in the experiments, there is an *increase* in threshold nonlinearity from κ to $(31/25)\kappa$. Given the measured single-beam MI threshold of $0.9kV$, the predicted double-beam threshold of $1.12kV$ matches the observed value.

2.5.3 Holographic Readout of Dynamics

The different behaviors above and below the modulation threshold are the result of different nonlinear dynamics within the initial distribution. Experimentally, we can observe this by taking advantage of the slow photorefractive response time of SBN and recording a volume hologram of the interactions. Subsequently, we can block one of the beams and use the other as a probe of the coupling, observing the energy transfer that would have happened if the other beam were present [41]. These holographic reconstructions are shown in Figs. 2.7(c,f,i). For linear propagation [Fig. 2.7(c)], each beam maintains its Gaussian form, as there is no nonlinear intensity interaction to induce an index change. By contrast, there are significant changes in the nonlinear cases. For weak coupling [Fig. 2.7(f)], light originally in the perturbative bump (shown in red) is seen to flow towards lower momentum states, while light from the equilibrium distribution (shown in blue) scatters in the opposite direction. For strong coupling [Fig. 2.7(i)], the momentum transfer is *asymmetric*. The thermal light is unchanged, while the non-thermal distribution looks *bimodal*, with half the intensity in the original angled hump and half centered at $\langle k\rangle = 0$, beyond the initial instability range of positive slope.

At this point, it is useful to revisit the plasma correspondence and interpret the scattering dynamics from a quasi-particle (speckle) perspective. From this viewpoint, the instability mechanism is essentially a resonant process, in which small-scale wavepackets generate and interact with large-scale modulations [41, 14]. The coupling threshold $\alpha\lambda_D \approx 1$ then separates the dynamics between regimes of weak and strong spatial turbulence. Indeed, weak (quasilinear) turbulence theory in plasma is characterized by the formation of a k-space plateau and the bidirectional transfer of momentum between the thermal and non-thermal distributions

[8, 45]. In the theory of strong turbulence, the thermal, non-resonant distribution is unchanged but the resonant distribution is greatly affected by wave-wave interactions [9]. In this case, there should be a direct transfer of momentum towards large scales ($\langle k \rangle = 0$), a stimulated scattering process known as Langmuir condensation in plasma physics [9, 10]. All of this is consistent with the observations in Figs. 2.7 (f) and (i). To the authors' knowledge, these internal dynamics have not been observed in material plasma.

2.5.4 Multiple Bump-on-Tail Instability and Long-Range Turbulence Spectra

Above the threshold $\alpha\lambda_D \sim 1$, the dynamics of the single BOT instability suggested that there is a turbulent breakdown of the quasi-linear plateau over the resonant range of k-vectors. However, the wavenumber region is too small to conclude that there is a self-similar spectrum between the humps. To extend the range, we add a third hump to the system, as described in Fig. 2.6.

Experimental results for the weak-coupling case are shown in Figs. 2.7(j) and 2.7(k). The output intensity remained uniform, up to unavoidable striations in the crystal, while the energy spectrum underwent significant redistribution due mode coupling. As the nonlinear interaction strength (applied voltage) was increased, the spectral bumps were observed to flatten. In all cases, the profile flattening was sequential, with lower momenta reaching a plateau first. This observation agrees with the simulations in Fig. 2.5 and supports the general conclusion that the final state of the system depends on the temporal sequence of wave diffusion [46, 6]. To our knowledge, this is the first demonstration of a multiple bump-on-tail instability and its associated competition of growth rates. Similar behavior should occur in any wave-kinetic system obeying Eq. (2.4), such as material plasma and cold atoms at finite temperature.

More complex behavior occurs for higher nonlinearity (Figs. 2.7(l) and 2.7(m)). In the strong coupling regime [14, 15, 1, 2, 3], modulations start to appear in intensity and momentum transfer continues beyond the plateau (zero-gradient) limit (though the inertial approximation is still valid [14, 4]). As before, wave-wave coupling is the dominant process of energy/momentum exchange [10, 9, 6]. A closer examination of this spectrum, shown in Fig. 2.9, reveals a self-similar profile with a k^{-2} fall-off. This algebraic spectrum holds for the entire wavenumber range between the first and last peaks, despite the fact that the central hump provided an initial region of stability ($\partial f_0/\partial k < 0$).

The intensity waves present in the strong-coupling regime (Fig. 2.7(l)) are suggestive of solitons and, indeed, an ensemble of solitons can give the observed power spectrum [47]. For N solitons occupying a space of length L in 1D, having random phases and positions and maintaining total energy E_S, the Wigner spectrum:

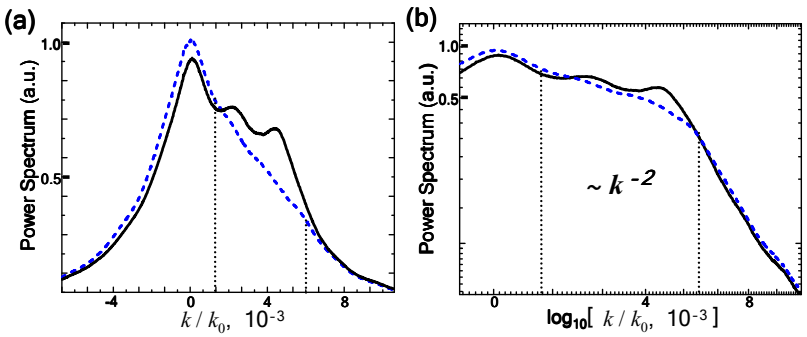

Fig. 2.9 Detailed look at the asymptotic spectral profile of the turbulent state during multiple BOT instability. (a) Comparison of input (solid) and output (dashed) profiles. (b) Comparison in log space, showing algebraic spectrum in interaction region.

$$\langle f_k \rangle \propto \frac{1}{L} \int_{N_{min}}^{N_{max}} dN\, N \wp(N) \left[\cosh(kN/E_S) \right]^{-2}, \tag{2.37}$$

where $\wp(N)$ is the probability for the system to be in the N-soliton state and $N_{min} \leq N \leq N_{max}$ due to soliton merging and turbulent redistribution. Choosing $N_{max} \sim E_S/k$ (using the condition of close packing) and replacing the $\cosh^{-2}$ term in (2.37) by a step function yields $\langle f_k \rangle \propto \frac{1}{L} \int_{N_{min}}^{E_S/k} dN\, N \wp(N)$. For the case when all states are occupied uniformly [$\wp(N)$ =const], $\langle f_k \rangle \propto k^{-2}$.

Interestingly, the equipartition spectrum k^{-2} observed experimentally in Section 2.5.4, is robust and appears in several different contexts of strong wave coupling. For example, dynamics with phase-dependent coupling — *e.g.*, four-wave mixing — can give an effective wave collision term that leads asymptotically to a k^{-2} spectrum [48, 49, 50]. For the phase-independent coupling here, the intensity-induced interactions are enough to drive the dynamics. Indeed, similar conservation arguments on the photonic plasmons (speckles), rather than number of solitons, also leads to a Rayleigh-Jeans distribution [48, 49, 50] $f_k = T/\left(k^2 - \mu\right)$, where the effective temperature $T \propto l_c^{-2}$ and the effective chemical potential μ is given by the average propagation constant (energy eigenvalue) of the waves. Note, however, that there must be a sufficient density of modes to achieve the equipartition. For example, the presence of (incoherent) solitons — *e.g.* from modulation instability — is not enough to guarantee equipartition. There must be enough interaction and propagation distance (evolution time) to go beyond soliton clustering [11] and cascade the interactions [12, 13]. Here, we encourage the wave-mixing cascade by seeding a quasi-thermal background distribution with additional non-equilibrium humps.

2.6 Discussion and Conclusions

In conclusion, we have treated the nonlinear propagation of statistical light as a photonic plasma of interacting speckles. A general Bohm-Gross dispersion relation was derived, allowing the identification of both a plasma frequency and a Debye length. These determined the nonlinear propagation constant and scale of wave dephasing, respectively. This approach unified previous observations using partially coherent light, such as nonlinear diffraction and incoherent modulation instability, and predicted a new class of optical phenomena. As representative examples, we considered single and multiple bump-on-tail instabilities. Optical methods of measurement, such as holography, allowed observation of dynamical behavior that had been predicted, but not observed, in material plasma. This included equal and opposite momentum exchange for weak nonlinear coupling and evidence for wave condensation for strong coupling. In the latter regime, wave-wave interactions caused the humped power spectrum to merge into a single-peaked profile, with an algebraic k^{-2} spectrum in the inertial range. This profile, and its associated intensity modulations, is the hallmark signature of optical Langmuir turbulence. The results extend plasma dynamics beyond their fluid context and show clearly that there is much potential for controlling correlation dynamics and optical energy distributions using plasma-type wave phenomena.

Acknowledgements We thank P.H. Diamond, C. Sun, and L.I. Dylova for very valuable discussions. This work was supported by the NSF, DOE and AFOSR.

References

1. A.A. Vedenov, L.I. Rudakov, Dokl. Akad. Nauk SSSR **159**, 767 (1964). DOI OSTI-ID-4648594
2. A.A. Vedenov, A.V. Gordeev, L.I. Rudakov, Plasma Physics **9**(6), 719 (1967). URL http://stacks.iop.org/0032-1028/9/719
3. M. Soljacic, M. Segev, T. Coskun, D.N. Christodoulides, A. Vishwanath, Phys. Rev. Lett. **84**(3), 467 (2000). DOI 10.1103/PhysRevLett.84.467
4. D. Kip, M. Soljacic, M. Segev, E. Eugenieva, D.N. Christodoulides, Science **290**(5491), 495 (2000). DOI 10.1126/science.290.5491.495. URL http://www.sciencemag.org/cgi/content/abstract/290/5491/495
5. U. Frisch, *Turbulence: The Legacy of A.N. Kolmogorov* (Cambridge University Press, Cambridge, 1995)
6. B.B. Kadomtsev, *Plasma Turbulence*, vol. 1 (Academic Press, London, New York, 1965)
7. S. Jia, W. Wan, J.W. Fleischer, Opt. Lett. **32**(12), 1668 (2007). URL http://ol.osa.org/abstract.cfm?URI=ol-32-12-1668
8. N.A. Krall, A.W. Trivelpiece, *Principles of Plasma Physics* (McGraw-Hill, New York, 1973, 1973)
9. M.V. Goldman, Rev. Mod. Phys. **56**(4), 709 (1984). DOI 10.1103/RevModPhys.56.709
10. P.A. Robinson, Rev. Mod. Phys. **69**(2), 507 (1997). DOI 10.1103/RevModPhys.69.507
11. Z. Chen, S.M. Sears, H. Martin, D.N. Christodoulides, M. Segev, Proceedings of the National Academy of Sciences of the United States of America **99**(8), 5223 (2002). DOI 10.1073/pnas.072287299. URL http://www.pnas.org/content/99/8/5223.abstract

12. V.N. Tsytovich, preprint, Academy of Sciences, USSR, [SOV PHYS USPEKHI, 1973, 15 (5), 632650] (150) (1969)
13. S.I. Popel, V.N. Tsytovich, S.V. Vladimirov, Physics of Plasmas **1**(7), 2176 (1994). DOI 10.1063/1.870617. URL http://link.aip.org/link/?PHP/1/2176/1
14. D.V. Dylov, J.W. Fleischer, Phys. Rev. Lett. **100**(10), 103903 (2008). DOI 10.1103/PhysRevLett.100.103903. URL http://link.aps.org/abstract/PRL/v100/e103903
15. D.V. Dylov, J.W. Fleischer, Phys. Rev. A (Atomic, Molecular, and Optical Physics) **78**(6), 061804 (2008). DOI 10.1103/PhysRevA.78.061804. URL http://link.aps.org/abstract/PRA/v78/e061804
16. W. Wan, S. Jia, J.W. Fleischer, Nat Phys **3**, 2007/01//print (2007). DOI 10.1038/nphys486. URL http://dx.doi.org/10.1038/nphys486
17. R. Dong, C.E. Rüter, D. Kip, O. Manela, M. Segev, C. Yang, J. Xu, Phys. Rev. Lett. **101**(18), 183903 (2008). DOI 10.1103/PhysRevLett.101.183903. URL http://link.aps.org/abstract/PRL/v101/e183903
18. D.V. Dylov, J.W. Fleischer, Opt. Lett. **34**(17), 2673 (2009). URL http://ol.osa.org/abstract.cfm?URI=ol-34-17-2673
19. A.V. Mamaev, M. Saffman, A.A. Zozulya, Phys. Rev. Lett. **76**(13), 2262 (1996). DOI 10.1103/PhysRevLett.76.2262
20. T. Bohr, M.H. Jensen, G. Paladin, A. Vulpiani, *Dynamical Systems Approach to Turbulence*, *Cambridge Nonlinear Science Series*, vol. 8 (Cambridge University Press, Cambridge, England, 1998, 1998)
21. D.N. Christodoulides, E.D. Eugenieva, T.H. Coskun, M. Segev, M. Mitchell, Phys. Rev. E **63**(3), 035601 (2001). DOI 10.1103/PhysRevE.63.035601
22. E. Wigner, Phys. Rev. **40**(5), 749 (1932). DOI 10.1103/PhysRev.40.749
23. J.E. Moyal, Mathematical Proceedings of the Cambridge Philosophical Society **45**(01), 99 (1949). DOI 10.1017/S0305004100000487
24. B. Hall, M. Lisak, D. Anderson, R. Fedele, V.E. Semenov, Phys. Rev. E **65**(3), 035602 (2002). DOI 10.1103/PhysRevE.65.035602
25. L. Helczynski, D. Anderson, R. Fedele, B. Hall, M. Lisak, IEEE J. Sel. Top. Quantum Electron. **8**(3), 408 (2002). DOI 10.1109/JSTQE.2002.1016342
26. V.V. Shkunov, D.Z. Anderson, Phys. Rev. Lett. **81**(13), 2683 (1998). DOI 10.1103/PhysRevLett.81.2683
27. D.N. Christodoulides, T.H. Coskun, M. Mitchell, M. Segev, Phys. Rev. Lett. **78**(4), 646 (1997). DOI 10.1103/PhysRevLett.78.646
28. S.V. Bulanov, M. Yamagiwa, T.Z. Esirkepov, D.V. Dylov, F.F. Kamenets, et al., Plasma Physics Reports **32**(4), 263 (2006)
29. S.V. Bulanov, D.V. Dylov, T.Z. Esirkepov, F.F. Kamenets, D.V. Sokolov, Plasma Physics Reports **31**(5), 369 (2005)
30. R. Fedele, D. Anderson, Journal of Optics B: Quantum and Semiclassical Optics **2**(2), 207 (2000). URL http://stacks.iop.org/1464-4266/2/207
31. W. Martienssen, E. Spiller, American Journal of Physics **32**(12), 919 (1964). DOI 10.1119/1.1970023. URL http://link.aip.org/link/?AJP/32/919/1
32. A. Picozzi, Opt. Express **15**(14), 9063 (2007). URL http://www.opticsexpress.org/abstract.cfm?URI=oe-15-14-9063
33. G.E. Vekstein, American Journal of Physics **66**(10), 886 (1998). DOI 10.1119/1.18978. URL http://link.aip.org/link/?AJP/66/886/1
34. S.L. Musher, A.M. Rubenchik, V.E. Zakharov, Physics Reports **252**(4), 177 (1995). DOI 10.1016/0370-1573(94)00071-A
35. C. Sun, D.V. Dylov, J.W. Fleischer, Opt. Lett. **34**(19), accepted (2009)
36. M. Lisak, D. Anderson, L. Helczynski-Wolf, P. Berczynski, R. Fedele, V. Semenov, Physica Scripta **T113**, 56 (2004). URL http://stacks.iop.org/1402-4896/T113/56
37. D. Anderson, B. Hall, M. Lisak, M. Marklund, Phys. Rev. E **65**(4), 046417 (2002). DOI 10.1103/PhysRevE.65.046417
38. V. Arunasalam, American Journal of Physics **36**(7), 601 (1968). DOI 10.1119/1.1975025. URL http://link.aip.org/link/?AJP/36/601/1

39. D. Anderson, L. Helczynski-Wolf, M. Lisak, V. Semenov, Phys. Rev. E **69**(2), 025601 (2004). DOI 10.1103/PhysRevE.69.025601
40. S. Pitois, S. Lagrange, H.R. Jauslin, A. Picozzi, Phys. Rev. Lett. **97**(3), 033902 (2006). DOI 10.1103/PhysRevLett.97.033902. URL http://link.aps.org/abstract/PRL/v97/e033902
41. C. Anastassiou, M. Segev, K. Steiglitz, J.A. Giordmaine, M. Mitchell, M. feng Shih, S. Lan, J. Martin, Phys. Rev. Lett. **83**(12), 2332 (1999). DOI 10.1103/PhysRevLett.83.2332
42. C. Anastassiou, J.W. Fleischer, T. Carmon, M. Segev, K. Steiglitz, Opt. Lett. **26**(19), 1498 (2001). URL http://ol.osa.org/abstract.cfm?URI=ol-26-19-1498
43. D.N. Christodoulides, M.I. Carvalho, J. Opt. Soc. Am. B **12**(9), 1628 (1995). URL http://josab.osa.org/abstract.cfm?URI=josab-12-9-1628
44. Z. Chen, J. Klinger, D.N. Christodoulides, Phys. Rev. E **66**(6), 066601 (2002). DOI 10.1103/PhysRevE.66.066601
45. A.N. Kaufman, Journal of Plasma Physics **8**(01), 1 (1972). DOI 10.1017/S0022377800006887
46. N.J. Fisch, J.M. Rax, Physics of Fluids B: Plasma Physics **5**(6), 1754 (1993). DOI 10.1063/1.860809. URL http://link.aip.org/link/?PFB/5/1754/1
47. A.S. Kingsep, L.I. Rudakov, R.N. Sudan, Phys. Rev. Lett. **31**(25), 1482 (1973). DOI 10.1103/PhysRevLett.31.1482
48. S. Dyachenko, A.C. Newell, A. Pushkarev, V.E. Zakharov, Physica D **57**(1–2), 96 (1992). DOI 10.1016/0167-2789(92)90090-A
49. V.M. Malkin, Phys. Rev. Lett. **76**(24), 4524 (1996). DOI 10.1103/PhysRevLett.76.4524
50. A. Picozzi, Opt. Express **15**(14), 9063 (2007). DOI 10.1364/OE.15.009063. URL http://www.opticsexpress.org/abstract.cfm?URI=oe-15-14-9063

http://www.springer.com/978-3-642-16548-1

Localized States in Physics: Solitons and Patterns

Descalzi, O.; Clerc, M.G.; Residori, S.; Assanto, G. (Eds.)

2011, XVIII, 286 p., Hardcover
ISBN: 978-3-642-16548-1